Investigation of microstructure defects in EUROFER97 under He^+/Fe^{3+} dual ion beam irradiation

B. Kaiser[*,a], E. Gaganidze[a], C. Dethloff[a], R. Schwaiger[a], D. Brimbal[b], M. Payet[b], L. Beck[b], J. Aktaa[a]

[a] Karlsruhe Institute of Technology, Institute for Applied Materials (IAM), Hermann-von-Helmholtz Platz 1, Eggenstein-Leopoldshafen 76344, Germany
[b] CEA, DEN, Service de Recherches de Métallurgie Physique, Laboratoire JANNUS, Gif-sur-Yvette F-91191, France

ABSTRACT

Fusion like conditions for reduced activation ferritic/martensitic steels in the first wall are simulated with single Fe^{3+} and He^+/Fe^{3+} dual ion beam irradiation of EUROFER97 at the Jannus laboratory, CEA Saclay, introducing a damage of 16 dpa and a helium content up to 260 appm. The samples are irradiated at temperatures of 330 °C, 400 °C and 500 °C. The quantitative determination of size distribution and density of dislocation loops is obtained using weak-beam dark-field imaging mode. Burgers vectors of $\frac{a0}{2}\langle 111 \rangle$ are observed for the majority of dislocation loops at irradiation temperatures of 330 °C and 400 °C. At 500 °C no dislocation loops are found. The impact of single and dual ion beam irradiation on mechanical properties is determined by means of nanoindentation. An increase in nano-hardness of up to 35% due to irradiation was measured at samples irradiated at 400 °C. A kinetic rate model is applied for the description of nucleation and evolution of helium bubbles and compared with the experimental results. Evaluating the rate model with help of TEM-results for size and density of bubbles indicates the nucleation scheme as the main source for quantitative disagreement between the model and irradiation.

1. Introduction

The efficient operation of future fusion power plants relies critically on the life time and durability of materials exposed to the expected harsh conditions. In particular, the first wall has to endure a high flux of neutrons at elevated temperatures leading to severe degradation and change in material properties [1,2]. Therefore, it is of great importance to predict precisely the impact of radiation induced damage and to include its implications properly in the design. However, until the start of IFMIF no material radiation program can provide the 14 MeV neutrons released by the deuterium-tritium fusion [3]. At the moment, material testing for fusion devices uses mainly fast and mixed spectra fission reactors, which can create as well high numbers of atomic displacements. In addition, nuclear transmutations and the resulting gas production enabled by 14 MeV neutrons are mimicked by doping techniques [4]. Due to the high penetration depths of neutrons, the spatially homogeneous irradiation of specimens for mechanical tests is obtained and allows the reliable characterisation of the radiation impact on mechanical properties, e.g. yield strength, elongation, toughness etc. [5]. Apart from fission neutron reactors recently self ion irradiation combined with previous or simultaneous gas implantation receive popularity for the emulation of 14 MeV fusion neutrons [6,7].

Compared to fast neutrons ion irradiation profits from low cost and time consumption and facilitated specimen handling due to the avoided activation. In particular, the high damage rates increase the attractiveness of ion irradiation as a screening method and thus promise an immense speed up of material development and validation [8]. Nevertheless, ion irradiation still has to deal with two major issues: first, the precise determination of differences and artefacts compared to neutrons caused by the high dpa rates and, second, the reliable mechanical characterisation of an inhomogeneous damage layer covering a thickness of 1–2 μm.

In order to investigate dpa and helium effects at fusion relevant helium to dpa ratios for first wall application we apply Fe^{3+}/He^+ dual beam irradiation on the reduced activation ferritic/martensitic steel EUROFER97. The post irradiation examination includes TEM analysis of dislocation loops, mechanical characterisation by means of nanoindentation and modelling of helium bubble nucleation and growth by kinetic reaction rates.

Because EUROFER97 is currently subject to several neutron irradiation programmes including post irradiation microstructure analysis and mechanical characterisation, the literature provides a lot of data for comparison with dual ion beam irradiation [5,9–12]. Concerning the high dpa-rates and consequently short irradiation time of ions the

appearance of a similar microstructure evolution usually requires a higher temperature compared to neutrons, commonly denoted as temperature shift [13]. Therefore, analysing the temperature dependence of voids or dislocation loops in general allows to identify dpa-rate effects. Additionally, the development and application of a kinetic rate model shall support the interpretation of experiments and the identification of responsible mechanisms for dpa-rate effects.

2. Dual ion beam irradiation and sample preparation

The 25 mm thick EUROFER97 plates were produced by Böhler Austria GmbH. The final heat treatment applied by the manufacturer includes a normalisation at 980 °C for 0.5 h and tempering at 760 °C for 1.5 h. For the ion irradiation discs of 3 mm diameter and approximately 90 μm thickness were prepared. The irradiation with 1.2 MeV He^+ and 3.0 MeV Fe^{3+} ions was performed at the JANNUS Facility at Saclay [14,15]. The simultaneous dual ion beam irradiation was carried out at temperatures of 330 °C, 400 °C and 500 °C. We achieved a broadened implantation profile of helium by inserting aluminium energy degraders into the beam. Additionally, reference irradiations with Fe^{3+} single ion beam were performed at 290 °C and 400 °C.

In order to choose ion doses which lead to damage and helium concentration ratios similar to conditions expected in future fusion reactors, the stopping range and vacancy creation was calculated with SRIM [16]. Fig. 1 displays the expected depth profiles of damage and helium concentration for the applied doses of $1.8 \cdot 10^{16}$ $Fe^{3+}cm^{-2}$ and $7.2 \cdot 10^{15}$ He^+cm^{-2}. Thus, fusion like conditions are obtained at depths between 500 nm and 800 nm from the surface where the applied fluxes lead to 15 dpa/260 appm He and a helium-dpa ratio of 17 appm He/ dpa. Unfortunately, the dual beam irradiation was affected by insufficient control and monitoring of the ion flux leading to large uncertainties of $-16\%/+24\%$ in the doses. The single ion beam irradiation achieved 26 dpa.

Cross-section TEM samples were prepared via focused-ion-beam (FIB) machining, followed by subsequent cleaning with 300 eV Argon ions to reduce the FIB damage. In this manner we can directly access the damage profile and ensure that the TEM analysis covers the region between 500 nm and 800 nm.

3. Dislocation loops characterisation by Weak-beam dark-field imaging

Dislocation loops originate from the clustering of self interstitial atoms and are known as the main source for irradiation hardening. We apply the TEM Weak-beam dark-field (WBDF) technique to determine Burgers vector **b**, density and size of dislocation loops. Micrographs in Fig. 2 show dislocation loops at temperatures of 330 °C and 400 °C with

excitation of the reciprocal lattice vector **g** = {310}. At an irradiation temperature of 500 °C we did not find any dislocation loops. Apart from loops, strain fields of dots and dislocation lines lead to observed contrast in WBDF. The identification of loops is complicated by the interference with dislocation lines and noise. In particular, a loop shape is hardly resolvable for features smaller than 2 nm and cannot be distinguished from dot like defects. Thus, the subsequent quantification is limited to features clearly identified as loops.

The invisibility criteria **b·g** = 0 implies that only a certain fraction of loops with a particular Burgers vector appears. In case of the evaluated WBDF images g(3g) condition are maintained for lattice vectors {200}, {121} and {310}. Following [17], measured loop densities for each lattice vector and the invisibility criteria define an equation system which allows the determination of real loop densities for the Burgers vectors $a_0\langle100\rangle$ and $\frac{a_0}{2}\langle111\rangle$ by the least square solution. Results at 330 °C and 400 °C are summarised in Table 1. With increasing irradiation temperature the density of loops slightly decreases from $8.5 \cdot 10^{21}\,m^{-3}$ to $7.3 \cdot 10^{21}\,m^{-3}$ whereas the size increases from 4.2 nm to 6.1 nm. At both temperatures 330 °C and 400 °C Burgers vectors $\frac{a_0}{2}\langle111\rangle$ dominate with a fraction of 71% and 78%, respectively.

The temperature dependence of dislocation loops for fast neutron irradiation up to 16 dpa of EUROFER97 is discussed in [11,18]: a high density of loops of approximately 10^{22} m^{-3} is observed at low irradiation temperatures of 250 °C–330 °C, followed by a decrease of two orders of magnitude for a further temperature increase to 450 °C. Note, that the density of loops at 450 °C of 10^{19} m^{-3} is very close to the detection limit for the volume of a cross-section lamella with an 1 μm large damage layer. The reported behaviour is quite similar to the temperature dependence observed in the present dual ion beam irradiation experiment, however, the steep drop of dislocation density is observed between 400 °C and 500 °C. Thus, a temperature shift due to different dpa-rates between ion and neutron irradiation is observed for two characteristic features of the temperature dependence of dislocation loops. First, the temperature interval of a high density of loops shifted from [250 − 330] °C to [330 − 400] °C. Second, a recovered matrix with no loops with respect to the detection limit is found at 500 °C for ion irradiation instead of 450 °C in case of neutrons. We conclude therefore a temperature shift of 50 °C–70 °C between neutron and the present ion irradiation.

4. Irradiation hardening by nanoindentation

Irradiation is known to influence mechanical properties. In particular, irradiation hardening originates from interstitial defects and is usually characterised by an increase in yield strength. For small damage layers induced by ion beam irradiation the evaluation of suitable mechanical characterisation for engineering needs is still under
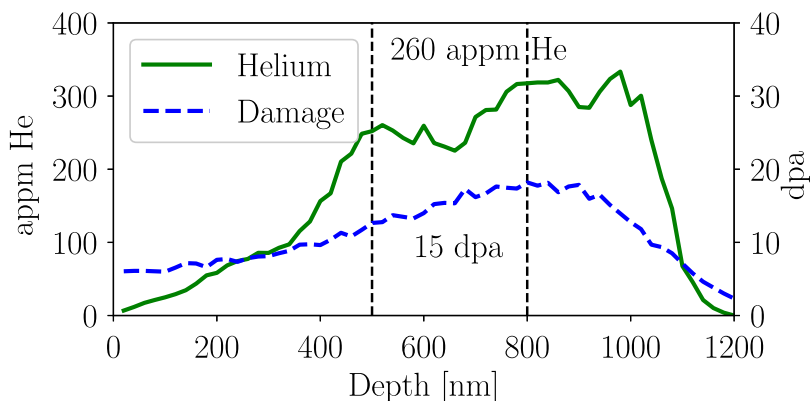

Fig. 1. SRIM calculation of the damage and helium concentration profile achieved after 6 h of 1.2 MeV He and 3.0 MeV Fe^{3+} ion irradiation with respective doses of $1.8 \cdot 10^{16}$ $Fe^{3+}cm^{-2}$ and $7.2 \cdot 10^{16}$ $Hecm^{-2}$. The desired damage and helium content of approximately 16 dpa and 260 appm He is obtained at implantation depths in between 500 nm and 800 nm.
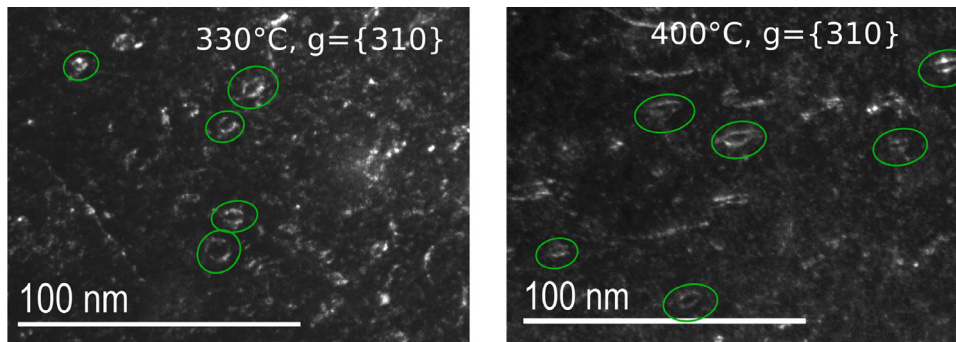
Fig. 2. Weak-beam dark-field images for g(3g) diffraction condition with g = {310} for irradiation temperatures of 330 °C (left) and 400 °C (right). Some dislocation loops are marked by green ellipses. (For interpretation of the references to colour in this figure legend, the reader is referred to the web version of this article.)

Table 1
Summary of dislocation loop properties after irradiation to 16 dpa and 260 He appm at 330 °C and 400 °C.

	330 °C	400 °C
C_{loops}	$8.5 \cdot 10^{21}\,\mathrm{m}^{-3}$	$7.3 \cdot 10^{21}\,\mathrm{m}^{-3}$
$a_0 \langle 100 \rangle$	29%	22%
$\frac{a_0}{2} \langle 111 \rangle$	71%	78%
$\langle D \rangle$	4.2 nm	6.1 nm
Loops counted	185	274

development [19–21]. Apart from rarely applied micro-pillar compression [22] nanoindentation is frequently used on ion beam irradiated martensitic/ferritic alloys [6,23,24].

In the present study nanoindentation was conducted with an Agilent Technologies Nanoindenter G200 equipped with a Berkovich tip at 26 °C. The indentation strain-rate was set to 0.05 s^{-1} and the materials indented to a maximal indentation depth of 2 μm. Hardness is determined by means of continuous stiffness measurement [25]. The resulting hardness as a function of the contact depth is plotted in Fig. 3 for unirradiated EUROFER97 and EUROFER97 irradiated with single and dual ion beam at 400 °C. Already for unirradiated EUROFER97 the indentation size effect [26] results in increased hardness at indentation depth smaller the 400 nm. Recent investigations of Heintze and co-workers [21] suggest that the indentation size effect and irradiation hardening are not influencing each other and can be considered as a superposition for indentation depths larger than 300 nm. In addition to the indentation size effect, the irradiated samples exhibit a high amount of additional hardness at small indentation depths and converge for large indentation depth towards the bulk hardness. Thus, defining an indentation depth for the irradiation hardness measurement requires a compromise between indentation size effect and substrate effect. We choose 400 nm, because the indentation size effect in unirradiated EUROFER97 is mostly decayed but the region between 500 nm and 800 nm with the desired helium/dpa ratio still in the indentation probe volume. As summarised in Table 2, the single iron ion irradiation induced an additional hardening of 34%. Dual ion beam irradiation increased the hardness up to 25%. Due to different iron ion doses any influence of helium on hardness is not clearly identifiable. Nevertheless, considering dislocation loops as the main source for hardening, the results of the nanoindentation experiment are as expected, showing a stronger hardening at higher dpa values . This assumption is further confirmed by the TEM analysis of the dislocation loop density. For the present single beam 26 dpa irradiation at 400 °C reference [33] reports of a higher dislocation loop density of $3.6 \cdot 10^{22}$ m^{-3} with a larger mean diameter of 7.9 nm in comparison with the results of Table 1. In the framework of disperse barrier models the increase of density and size is associated with an increase in hardness.

Hardening caused by neutron irradiation of EUROFER97 was found at irradiation temperatures of 250 °C–350 °C, but not at 400 °C [18,27], indicating again a dpa-rate effect. Of course, it was reported that hardening is strongly correlated with high density of dislocation loops for neutrons as well as for ions. Therefore, the observed temperature shift in hardening is reflecting the rate effects on the density of dislocation loops.

5. Bubbles nucleation and growth

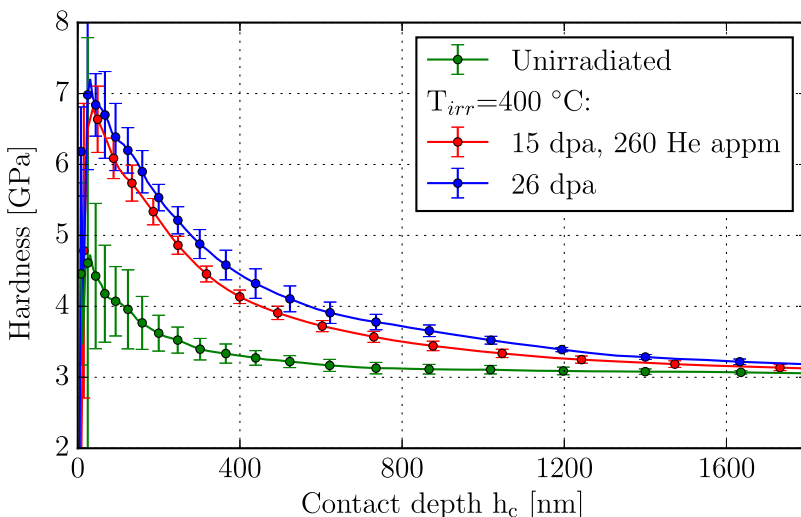We already reported on nucleation and growth of helium bubble for

Fig. 3. Hardening as a function of indentation depth of unirradiated (green) and irradiated EUROFER97. The irradiations were carried out at 400 °C with single Fe^{3+} ions to 26 dpa (blue) and He^{+}/Fe^{3+} ions to 16 dpa/260 He appm (red). (For interpretation of the references to colour in this figure legend, the reader is referred to the web version of this article.)

Table 2
Results for indentation hardening for ion irradiation at 400 °C at a contact depth of 400 nm.

	26 dpa	15 dpa 260 He appm
ΔH_{ref}	1.1 GPa (34%)	0.8 GPa (25%)

the present dual beam irradiation in [28]. It is known, that in general helium enhances the cavity formation. Remarkably, no cavity formation was observed for the case of single iron ion irradiation at 400 °C in [33]. Therefore, in the following we associate the cavities as helium bubbles. Bubbles were detected by TEM through focal series in bright field mode for all irradiation temperatures in case of dual ion beam irradiation as shown in Fig. 4. The application of a kinetic rate model on nucleation and growth shows qualitative agreement for temperature dependence of bubbles size and density with the irradiation experiment. However, quantitative disagreement with the experiment remained for bubble size and density as well as for helium absorption at extended defects like grain boundaries and dislocation lines. Below, a short recapitulation of the TEM findings and the model of reference [28] is followed by the recent progress in the validation our model with help of the dual beam results.

Fig. 4(a)–(c) show that we found homogeneously distributed

bubbles in the grains for all irradiation temperatures. Additionally, at 500 °C bubbles occur also at grain boundaries and dislocation lines as observed in Fig. 4(d), indicating the transition to heterogeneous bubble nucleation as found for neutron irradiation [10]. The histograms in Fig. 5 show the density distribution of homogeneously nucleated bubbles as a function of the bubble diameter for three irradiation temperatures as published in [28].

The kinetic rate model is described in details in refs. [28,29]. Due to the vacancy supersaturation during irradiation, helium atoms find easily a substitutional lattice site. Nucleation and growth of bubbles is modelled by the absorption and emission of substitutional helium from bubbles consisting of i helium and vacancies with the reaction k_i and g_i. Diffusion controlled absorption of helium-vacancy clusters is assumed for the determination of k_i.

$$k_i = 4\pi R_i D_{He}^{eff}(T_{irr}). \tag{1}$$

Thus, the rate k_i depends obviously on the cluster radius R_i and the effective vacancy assisted helium diffusion constant D_{He}^{eff} [30]. As common, the emission probability is derived from a steady state argumentation resulting in a relation between the equilibrium cluster concentration and the kinetic coefficients k_i and g_i.
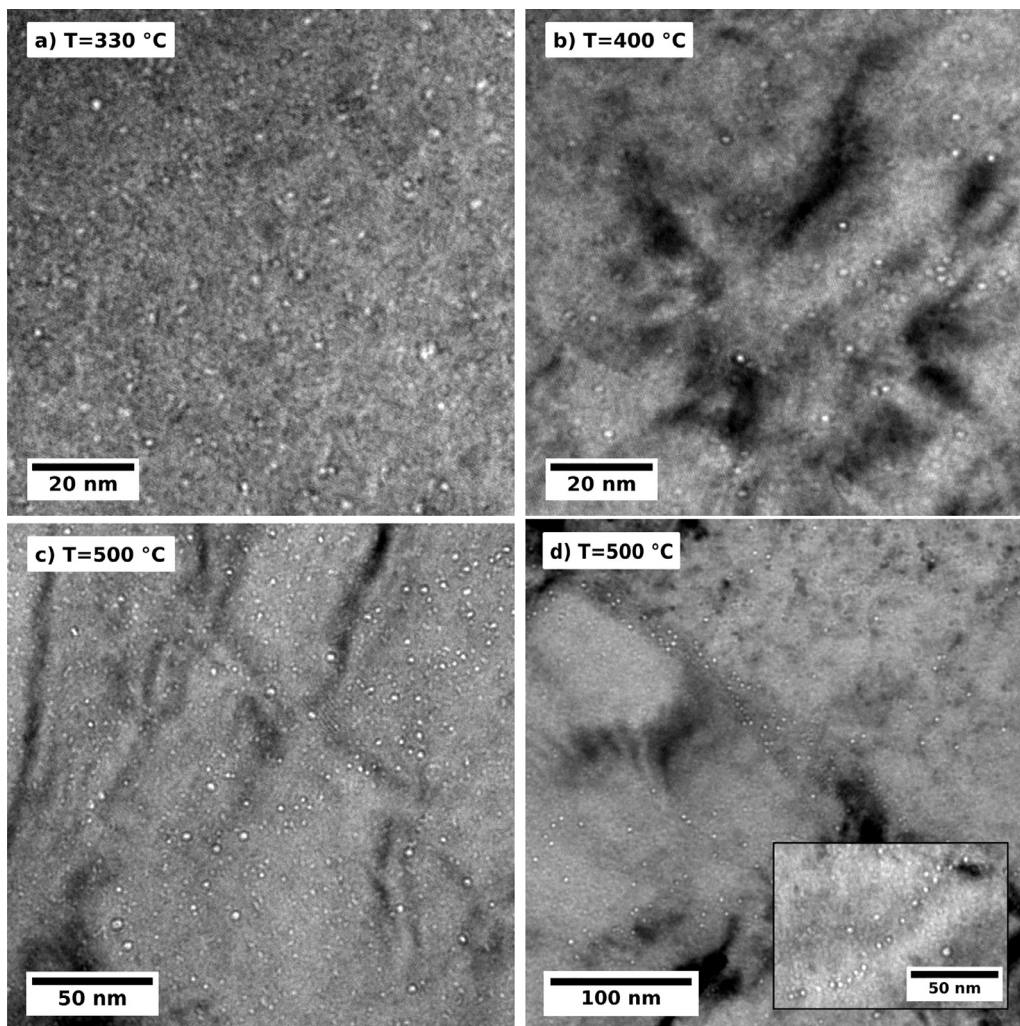

Fig. 4. TEM micrographs of helium bubbles after irradiation at 330 °C (a), 400 °C (b) and 500 °C (c + d). Spatially homogeneous distributions of bubbles are found for all irradiation temperatures (a–c). Additionally, spatially heterogeneous nucleation is observed at 550 °C in figure d). The high density of bubbles in the narrow band corresponds to cavity formation at grain boundaries. The inset in figure (d) shows bubbles in the grain characteristically lined up one after the other which indicates dislocation lines as origin for their formation. The respective underfocus is −0.5 μm in (a) and (b), −1.0 μm in (c) and −2 μm in (d).
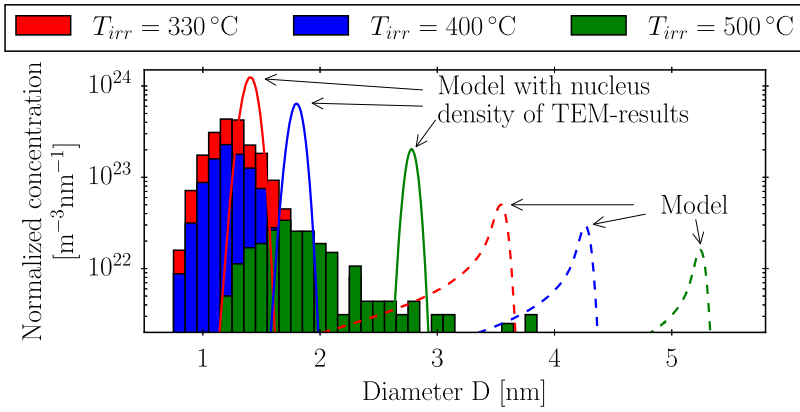
Fig. 5. Density of helium bubbles as a function of the bubble diameter for the irradiation temperatures of 330 °C, 400 °C and 500 °C. Quantitative characterisation of the TEM-micrographs are represented by the bar diagrams. For comparison, predictions of the kinetic rate model are plotted with dashed lines. Distributions plotted with solid lines are obtained by reducing the model to bubble growth. The bubble size distributions of the experiment (bar diagrams) and the model (dashed lines) are already published in [28].

$$g_i = k_i \Omega^{-1} \exp\left[-\frac{F_i^b}{k_B T_{irr}}\right]. \tag{2}$$

Here, F_i^b denotes the free binding energy, Ω the atomic volume and k_B the Boltzmann constant. The bindings energies for a substitutional helium atom are determined using the variable gap model [31]. The equations of motion for bubble concentrations C_i read as follows:

$$\frac{\partial C_1}{\partial t} = G_{He} - L_{Sinks} - \sum_{i \geq 1} k_i C_1 C_i + \sum_{i \geq 2} g_i C_i, \tag{3a}$$

$$\frac{\partial C_i}{\partial t} = -[k_i C_1 + g_i] C_i + g_{i+1} C_{i+1} + k_{i-1} C_1 C_{i-1}. \tag{3b}$$

The time evolution of concentration of C_1 is determined by Eq. (3a), accounting for the helium generation rate $G_{He}(t)$, losses at sinks L_{Sinks} and the absorption and emission of mobile units by clusters. The sink term L_{sink} accounts for the accumulation of helium at grain boundaries and dislocation lines. The losses of helium at extended defects are defined by

$$L_{sink} = D_{He}^{eff} C_1(t) [15/R_{gb}^2 + Z\rho_{dl}], \tag{4}$$

as given in ref. [32]. We reported in [28] that with the usage of reasonable parameters for sinks the model does not allow the homogeneous nucleation in the grains at all temperatures, due to the dominance of helium capture by sinks over helium bubble nucleation and growth. Therefore as a start, the results of the model presented in Fig. 5 by dashed lines neglect the influence of losses at extended defects.

Obviously, the model predicts larger bubbles and lower number density compared to the observation of the TEM. Nevertheless, the qualitative temperature dependence matches in most parts. The decreasing density with increasing temperature is found for the model as well as for the experiment. The prediction of larger bubbles with increasing temperature is experimentally only confirmed between 400 °C and 500 °C.

As a first assessment on which part of the model is responsible for the overestimation of the bubble size the nucleation scheme is close at hand, including the main assumptions and simplifications. In order to neglect the nucleation regime in the model we need a reasonable initial state $C_i^{initial}$ to start with the bubble growth. The choice of the initial state for the density distribution of bubbles is supported by the final bubble density observed by TEM and denoted as C_{TEM}. Because of the low nucleation rate during bubble growth it is well justified to approximate the density of nuclei with the final density of bubbles. Consequently, in the initial bubble distribution $C_i^{initial}$ we set the density for bubbles with the critical cluster size equal the final density observed with TEM. Because helium energetically stabilises the voids we assume that the critical cluster size is already achieved with the bond of two substitutional helium atoms resulting in $C_2^{initial} = C_{TEM}$. The start time t_{start} for the calculation ensures particle conservation implying equality

of helium introduced by irradiation and helium bound in nuclei and is defined by $G_{He} \cdot t_{start} = 2 \cdot C_2^{initial}$.

The results for the model using the nucleus density from TEM are plotted in Fig. 5 with solid lines. Obviously, the adapted nuclei density shifts the bubble diameters much closer to the results of the TEM-analysis and we can identify the nucleation scheme as a main source in our model for the quantitative overestimation in bubble size. Even though the shapes of the curves and the densities at the peak deviate from the experimental histograms, the total bubble density given by the area of the curves and histograms are identical as enforced by the initial state. The deviation is most likely mainly caused by the artificial initial state which is sharply peaked at the critical cluster size. However, at $T_{irr} = 500$ °C the bubble distribution gets much broader and exhibits a tail up to 4 nm, which is not reproduced by the model. Common explanation for ripening are bubble to void transition or coarsening by resolution of small bubbles.

So far we didn't account for the absorption of helium at extended sinks. Reasonable values for the sink strength of grain boundaries and dislocation lines in Eq. (4) are $R_{GB} = 0.5$ μm, $\rho_{disl} = 6.7 \cdot 10^{14}$ m^{-2} and $Z_{He} = 1.0$. The grain size R_{GB} resembles characteristic small lengths of the lath structure, because we detected bubbles even at the small angle boundaries of laths of the same block. The density for dislocation lines was determined by means of TEM in [33] in case of ion irradiation of EUROFER97 at 400 °C. Applying these parameters for the sinks strength in the model results in the suppression of homogeneous bubble nucleation in the grains and predicts extended defects as main site for nucleation [28]. With respect to recent evaluation of the nucleation scheme, it is interesting to check whether the absorption of helium at a nucleus density given by the TEM-results can compete against the sink strength of the grain boundaries and dislocation lines. It turned out that the model starting with the nucleus density obtained with TEM still results in homogeneous nano-sized bubbles in the matrix even in the presence of sinks. The amount of clusters absorbed at grain boundaries and dislocation lines rises with temperature from 10% at 330 °C to 32% at 500 °C as illustrated in Fig. 6. Helium content at both sink types is almost the same, because the chosen parameters result in similar sink strengths. However, the distributions for bubbles in the grain are almost not affected. Fig. 6 illustrates that the realignment of helium to sinks causes only a slightly shift to smaller sizes because the diameter scales with the third root of the number of helium vacancy clusters.

A detailed and conclusive comparison between model and experiment appears cumbersome, since the TEM-results are restricted to the qualitative observation of a transition from homogeneous to heterogeneous bubble formation. Nevertheless, the above discussed predictions of the model represent the same qualitative behaviour, since the helium absorbed at grain boundaries and dislocation lines increases with temperature. Additionally, the determined percentage of absorbed helium at grain boundaries and dislocation lines covers a range, which might be considered as reasonable to induce a transition from
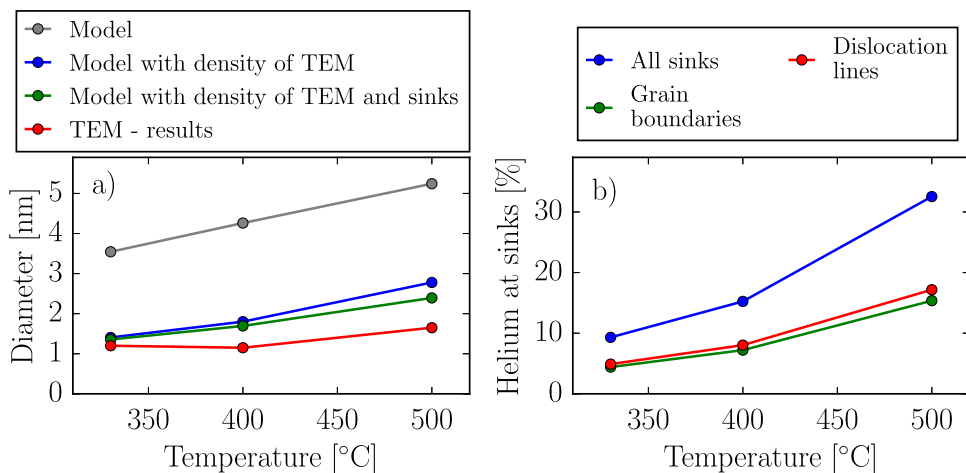
Fig. 6. (a): Final peak position of bubble size distribution as a function of irradiation temperature for several steps in the model evaluation (grey, blue and green) and the TEM-results (red). (b): Fraction of helium absorbed at extended defects as a function of irradiation temperature. (For interpretation of the references to colour in this figure legend, the reader is referred to the web version of this article.)

homogeneous to heterogeneous nucleation with respect to the TEM detection limit. More precise and quantitative TEM investigations of sink effects are desirable, but beyond the scope of the present work.

6. Conclusion

The present work covers the post irradiation examination of He^+/Fe^{3+} dual ion beam irradiation, including TEM analysis of dislocation loops and hardness measurement by means of nanoindentation. Dislocation loops are found for 330 °C and 400 °C, but not at 500 °C. The majority of dislocation loops has Burgers vector of type $\frac{a_0}{2}\langle 111\rangle$. In correlation to a high dislocation density at 400 °C the hardness measurement via nanoindentation indicates irradiation hardening of up to 34%. Comparing the findings for homogeneous/heterogeneous bubble nucleation, density of dislocation loops and hardening with neutron irradiation allows to identify dose rate effects and associate them with a temperature shift of 50°–70 °C. Additionally, a kinetic rate model for helium bubble nucleation and growth is evaluated with help of the experimental findings. Reducing the model on bubble growth improves the prediction on bubble size and nucleation at grain boundaries and dislocation lines at elevated temperatures.

References

[1] N. Baluc, Plasm. Phys. Controll. Fusion 48 (2006) B165.
[2] S. Zinkle, L. Snead, Annu. Rev. Mater. Res. 44 (2014) 241–267, http://dx.doi.org/10.1146/annurev-matsci-070813-113627.
[3] A. Möslang, C. R. Phys. 9 (2008) 457–468.
[4] S.J. Zinkle, A. Möslang, Fusion Eng. Des. 88 (2013) 472–482.
[5] E. Gaganidze, J. Aktaa, Fusion Eng. Des. 88 (2013) 118–128, http://dx.doi.org/10.1016/j.fusengdes.2012.11.020.
[6] E. Wakai, M. Ando, T. Sawai, K. Kikuchi, K. Furuya, M. Sato, K. Oka, S. Ohnuki, H. Tomita, T. Tomita, et al., J. Nucl. Mater. 356 (2006) 95–104, http://dx.doi.org/10.1016/j.jnucmat.2006.05.032.
[7] E. Getto, Z. Jiao, A. Monterrosa, K. Sun, G. Was, J. Nucl. Mater. 462 (2015) 458–469.
[8] G. Was, Z. Jiao, E. Getto, K. Sun, A. Monterrosa, S. Maloy, O. Anderoglu, B. Sencer, M. Hackett, Scr. Mater. 88 (2014) 33–36.
[9] O.J. Weiß, E. Gaganidze, J. Aktaa, J. Nucl. Mater. 426 (2012) 52–58, http://dx.doi.org/10.1016/j.jnucmat.2012.03.027.
[10] M. Klimenkov, A. Möslang, E. Materna-Morris, J. Nucl. Mater. 453 (2014) 54–59, http://dx.doi.org/10.1016/j.jnucmat.2014.05.001.
[11] M. Klimenkov, E. Materna-Morris, A. Möslang, J. Nucl. Mater. 417 (2011) 124–126, http://dx.doi.org/10.1016/j.jnucmat.2010.12.261. Proceedings of ICFRM-14
[12] E. Materna-Morris, A. Möslang, R. Rolli, H.C. Schneider, J. Nucl. Mater. 386–388 (2009) 422–425, http://dx.doi.org/10.1016/j.jnucmat.2008.12.157.
[13] L. Mansur, W. Coghlan, J. Nucl. Mater. 119 (1983) 1–25, http://dx.doi.org/10.1016/0022-3115(83)90047-8.
[14] L. Beck, Y. Serruys, S. Miro, P. Trocellier, E. Bordas, F. Leprêtre, D. Brimbal, T. Loussouarn, H. Martin, S. Vaubaillon, et al., J. Mater. Res. (2015) 1–12, http://dx.doi.org/10.1557/jmr.2014.414.
[15] Y. Serruys, P. Trocellier, S. Miro, E. Bordas, M. Ruault, O. Katasov, S. Henry, O. Leseigneur, T. Bonnaillie, S. Pellegrino, S. Vaubaillon, D. Uriot, J. Nucl. Mater. 386–388 (2009) 967–970, http://dx.doi.org/10.1016/j.jnucmat.2008.12.262. Proceedings of the Thirteenth International Conference on Fusion Reactor Materials
[16] J.F. Ziegler, Nucl. Instrum. Method B 219–220 (2004) 1027–1036, http://dx.doi.org/10.1016/j.nimb.2004.01.208. Proceedings of the Sixteenth International Conference on Ion Beam Analysis
[17] A. Prokhodtseva, B. Décamps, A. Ramar, R. Schäublin, Acta Mater. 61 (2013) 6958–6971, http://dx.doi.org/10.1016/j.actamat.2013.08.007.
[18] E. Materna-Morris, A. Möslang, H.C. Schneider, R. Rolli, Proceedings of 22nd IAEA Fusion Energy Conference, (2008), pp. 1–5.
[19] P. Hosemann, C. Shin, D. Kiener, J. Mater. Res. 30 (2015) 1231–1245.
[20] P. Hosemann, D. Kiener, Y. Wang, S.A. Maloy, J. Nucl. Mater. 425 (2012) 136–139, http://dx.doi.org/10.1016/j.jnucmat.2011.11.070.
[21] C. Heintze, F. Bergner, S. Akhmadaliev, E. Altstadt, J. Nucl. Mater. 472 (2016) 196–205, http://dx.doi.org/10.1016/j.jnucmat.2015.07.023.
[22] E. Grieveson, D. Armstrong, S. Xu, S. Roberts, J. Nucl. Mater. 430 (2012) 119–124.
[23] C. Heintze, F. Bergner, M. Hernandez-Mayoral, R. Kögler, G. Müller, A. Ulbricht, J. Nucl. Mater. 470 (2016) 258–267, http://dx.doi.org/10.1016/j.jnucmat.2015.12.041.
[24] M. Roldán, P. Fernández, J. Rams, D. Jiménez-Rey, C. Ortiz, R. Vila, J. Nucl. Mater. 448 (2014) 301–309, http://dx.doi.org/10.1016/j.jnucmat.2014.02.020.
[25] W. Oliver, G. Pharr, J. Mater. Res. 19 (2004) 3–20, http://dx.doi.org/10.1557/jmr.2004.19.1.3.
[26] G.M. Pharr, E.G. Herbert, Y. Gao, Annu. Rev. Mater. Res. 40 (2010) 271–292, http://dx.doi.org/10.1146/annurev-matsci-070909-104456.
[27] I. Sacksteder, H.C. Schneider, E. Materna-Morris, J. Nucl. Mater. 417 (2011) 127–130.
[28] B. Kaiser, C. Dethloff, E. Gaganidze, D. Brimbal, M. Payet, P. Trocellier, L. Beck, J. Aktaa, J. Nucl. Mater. 484 (2017) 59–67, http://dx.doi.org/10.1016/j.jnucmat.2016.11.014.
[29] C. Dethloff, E. Gaganidze, V.V. Svetukhin, J. Aktaa, J. Nucl. Mater. 426 (2012) 287–297, http://dx.doi.org/10.1016/j.jnucmat.2011.12.025.
[30] V. Borodin, P. Vladimirov, J. Nucl. Mater. 386–388 (2009) 106–108, http://dx.doi.org/10.1016/j.jnucmat.2008.12.070.
[31] T. Jourdan, J.P. Crocombette, J. Nucl. Mater. 418 (2011) 98–105, http://dx.doi.org/10.1016/j.jnucmat.2011.07.019.
[32] A.D. Brailsford, R. Bullough, Philos. Trans. R. Soc. A 302 (1981) 87–137, http://dx.doi.org/10.1098/rsta.1981.0158.
[33] D. Brimbal, L. Beck, O. Troeber, E. Gaganidze, P. Trocellier, J. Aktaa, R. Lindau, J. Nucl. Mater. 465 (2015) 236–244, http://dx.doi.org/10.1016/j.jnucmat.2015.05.045.